Environmental Science Nano

PAPER

View Article Online
View Journal | View Issue

Cite this: *Environ. Sci.: Nano*, 2018, 5, 2864

Facet-dependent generation of superoxide radical anions by ZnO nanomaterials under simulated solar light†

Qianwu Wang,‡[a] Huaxi Zhou,‡[b] Xinlei Liu,[a] Tong Li,[a] Chuanjia Jiang,[a] Weihua Song*[bc] and Wei Chen *[a]

Received 11th September 2018,
Accepted 6th November 2018

DOI: 10.1039/c8en01008k

rsc.li/es-nano

The capability of semiconductor nanomaterials to generate reactive oxygen species (ROS) under solar irradiation, which is critical for their photocatalytic applications and may affect their environmental implications, can be substantially influenced by intrinsic nanomaterial properties, particularly exposed facets. However, the specific mechanisms controlling the facet-dependent ROS generation of widely used semiconductor nanomaterials, *e.g.* zinc oxide (ZnO), are not well understood. Here, we report that under identical irradiation conditions a ZnO nanoplate material with predominantly exposed {0001} facets generates nearly four times as much superoxide radical anions ($O_2^{\bullet-}$) as a porous ZnO nanosheet material with predominantly exposed {10$\bar{1}$0} facets, even though the former possesses much smaller specific surface area. The enhanced $O_2^{\bullet-}$ generation of ZnO nanoplates with exposed {0001} facets can be ascribed to the following two aspects: (1) the {0001} facets, which contain more abundant coordinatively unsaturated zinc atoms, can adsorb a greater amount of molecular oxygen (O_2), and (2) the more negative conduction band potential of the {0001} facets can provide stronger thermodynamic driving force for the reduction of surface O_2 to $O_2^{\bullet-}$. The enhanced $O_2^{\bullet-}$ generation resulted in faster photocatalytic degradation of organic contaminants (using tetracycline as a model antibiotic contaminant) and greater bacterial inactivation (using *Escherichia coli* as a model microorganism). This study further identifies exposed facets as a critical nanomaterial property in dictating the photocatalytic activity and environmental implications of nanomaterials.

Environmental significance

The capability of semiconductor nanomaterials to generate reactive oxygen species (ROS) under solar irradiation is critical for their photocatalytic applications in pollutant degradation and disinfection, and may affect their implications in natural environments. The ROS generation pattern and rates of semiconductor nanomaterials can be substantially influenced by intrinsic nanomaterial properties. This study shows that nano-scale zinc oxide (ZnO), a widely used semiconductor nanomaterial, exhibits significant facet-dependent ROS generation properties, particularly regarding the different generation rates of superoxide radical anions. The findings will not only shed light on facet engineering of semiconductor nanomaterials with tunable ROS generation capabilities for environmental applications, but also contribute to more accurate delineation of the environmental implications of metal oxide nanomaterials.

1. Introduction

The last two decades have seen a boom in nanotechnology, and large quantities of engineered nanomaterials (ENMs) of various compositions are expected to be released into the environment with increasing fluxes.[1–3] The sustainable development of nanotechnology and human society as a whole requires a thorough understanding of the environmental and health implications of the ENMs.[4–7] Environmental toxicity and other biological effects of ENMs often involve the generation of reactive oxygen species (ROS), which is strongly influenced by environmental conditions, including environmental stimulants such as solar light irradiation.[8]

[a] *College of Environmental Science and Engineering, Ministry of Education Key Laboratory of Pollution Processes and Environmental Criteria, Tianjin Key Laboratory of Environmental Remediation and Pollution Control, Nankai University, Tianjin 300350, China. E-mail: chenwei@nankai.edu.cn; Fax: +86 22 85358169; Tel: +86 22 85358169*

[b] *Department of Environmental science & Engineering, Fudan University, Shanghai 200433, China. E-mail: wsong@fudan.edu.cn; Fax: +86 21 65642040; Tel: +86 21 65642040*

[c] *Shanghai Institute of Pollution Control and Ecological Security, 1515 North Zhongshan Road, Shanghai, 200080, P. R. China*

† Electronic supplementary information (ESI) available. See DOI: 10.1039/c8en01008k

‡ These authors contributed equally to this work.

As one of the most widely used ENMs, zinc oxide (ZnO) nanomaterials have found applications in numerous fields, such as cosmetics,[9] food packaging,[10] lasers,[11] solar cells,[12] piezoelectric transducers[13] and sensors.[14,15] Particularly, as a semiconductor, ZnO nanomaterials have been extensively investigated for photocatalytic disinfection or degradation of water pollutants under natural or simulated solar irradiation, which typically involves the generation of ROS such as superoxide radical anions ($O_2^{\bullet-}$), singlet oxygen ($^1O_2$), and hydroxyl radicals ($HO^{\bullet}$).[16–18] The capability of ZnO nanomaterials to generate ROS under solar irradiation is not only the basis for their applications in energy and environmental fields, but also a critical property affecting their environmental implications when they enter photic water bodies.[19,20]

Considering the importance of ROS generation in both photocatalytic applications and environmental implications of semiconductor nanomaterials such as ZnO, it is imperative to investigate how the intrinsic physicochemical properties of the nanomaterials can affect their capabilities to generate ROS, including the relative abundance and formation rates of different ROS species. Previous studies have established the relationships between the ROS generation of semiconductor nanomaterials and the size,[21] crystalline phase,[22,23] morphology,[24] as well as bulk or surface defects[19,25,26] of these nanomaterials. However, only a very limited number of studies have discussed the effects of exposed crystal facets on the formation of ROS,[27–29] and only two studies investigated facet-dependent ROS formation experimentally.[30,31] For example, it was shown that TiO_2 with higher proportion of exposed {001} facets could generate a greater amount of $O_2^{\bullet-}$ radicals.[30] In our previous study, we found that BiOI with predominately exposed {110} facets could generate $HO^{\bullet}$ radicals, whereas BiOI with predominately exposed {001} facets could not.[31] To date, facet-dependent ROS generation by ZnO nanomaterials has not been reported, and the knowledge acquired in the previous studies on the facet-dependent generation of ROS cannot be directly transferred to the case of ZnO nanomaterials under sunlight irradiation conditions, due to the differences in atomic composition and crystal structures between these materials.

The objective of this study was to understand how exposed facets of ZnO nanomaterials can affect the photochemical properties of these nanomaterials in aquatic environments. Herein, we selected ZnO as a model of n-type semiconductor material and synthesized two ZnO nanomaterials, including a ZnO nanoplate material with predominantly exposed {0001} facets and a nanosheet material with predominantly exposed {10$\bar{1}$0} facets. The types and quantities of photogenerated ROS by the two ZnO nanomaterials in aqueous matrices were examined under simulated solar irradiation. Strikingly, the two ZnO nanomaterials exhibited distinctly different capabilities to generate $O_2^{\bullet-}$ radical under simulated solar irradiation, which appeared to be facet-dependent. Thus, we further analyzed the surface adsorption properties, light absorption and charge carrier dynamics of the ZnO nanomaterials to elucidate the mechanisms controlling the facet-dependent photochemical ROS generation properties. Furthermore, the environmental implications of facet-dependent $O_2^{\bullet-}$ generation were illustrated by degradation of tetracycline, a model antibiotic contaminant, and inactivation of *Escherichia coli* (*E. coli*), a model microorganism, by the two ZnO materials under simulated solar light.

2. Experimental

2.1 Materials

All chemicals were directly used after purchase without further purification. Zinc acetate dihydrate ($(CH_3COO)_2Zn{\cdot}2H_2O$, ≥99%), triethanolamine (TEOA), 1,4-benzoquinone (BQ), isopropyl alcohol (IPA), thiourea (H_2NCSNH_2, ≥99%), sodium hydroxide and triethylenetetramine (≥99%) were purchased from Tianjin Chemical Reagent Co., Ltd. Sodium tartrate ($C_4H_4O_6Na_2{\cdot}2H_2O$, ≥99%) was obtained from Tianjin Oqi Medical Pharmaceutical Co., Ltd. Polyvinylpyrrolidone (PVP) and tetracycline were purchased from Beijing Solarbio Science & Technology Co., Ltd. 5,5-Dimethyl-1-pyrroline N-oxide (DMPO) was obtained from Shanghai Meryer Chemical Technology Co., Ltd. Furfuryl alcohol (FFA, 99%), terephthalic acid (TA), sodium dihydrogen phosphate (NaH_2PO_4) and disodium hydrogen phosphate (Na_2HPO_4) were purchased from Sigma-Aldrich. 2-Hydroxyl terephthalic acid (2HTA) was synthesized according to the literature.[32] Methanol (CH_3OH), acetonitrile (ACN) and trifluoroacetic acid (TFA) were HPLC grade and purchased from Concord Technology Co., Ltd. 2-Methyl-6-[*p*-methoxyphenyl]-3,7-dihydroimidazo[1,2-a]-pyrazin-3-one (MCLA) was purchased from TCI Chemicals. Deionized water was used throughout all the experiments.

2.2 Preparation of ZnO nanomaterials

Synthesis of ZnO with predominantly exposed {0001} facets. 0.8 g of $(CH_3COO)_2Zn{\cdot}2H_2O$, 0.4 g of NaOH and 0.1 g of PVP were dissolved in 40 mL of deionized water, stirred for 1 h at room temperature, and then transferred to a 50 mL Teflon-lined autoclave, which was sealed and kept at 180 °C for 24 h. After the hydrothermal reaction, the obtained white precipitate was isolated from the aqueous solution by centrifugation and subsequently washed with deionized water and absolute ethanol. Finally, the washed precipitate was dried at 60 °C for 12 h to obtain the ZnO-0001 material.

Synthesis of ZnO with predominantly exposed {10$\bar{1}$0} facets. 0.658 g of $(CH_3COO)_2Zn{\cdot}2H_2O$ and 0.1 g of $C_4H_4O_6Na_2{\cdot}2H_2O$ were dissolved in 40 mL of triethylenetetramine under vigorous stirring for 30 min at room temperature, and then 0.228 g of thiourea was added to the solution, followed by stirring for additional 30 min. The solution was transferred to a 50 mL Teflon-lined autoclave, which was sealed and maintained at 150 °C for 12 h. The white products were filtered, repeatedly washed with deionized water and absolute ethanol, and then dried at 60 °C for 12 h. Finally, the white products, which were identified as zinc sulfide from X-ray diffraction (XRD) (Fig. S1†), were heated in air at 600 °C for 4 h to obtain the ZnO-10$\bar{1}$0 material.

2.3 Characterization of ZnO nanomaterials

The crystal structures of the ZnO nanomaterials were characterized by XRD using a D/Max-2500 diffractometer (Rigaku, Tokyo, Japan) with Cu K_α radiation. The shape and morphology of the ZnO nanomaterials were characterized by scanning electron microscopy (SEM, Nova NanoSEM 230, FEI, Hillsboro, USA) and transmission electron microscopy (TEM, JEOL-2010, Japan) with an operating voltage of 200 kV. The Brunauer–Emmett–Teller (BET) specific surface area (SA_{BET}) of the ZnO nanomaterials was analyzed by nitrogen adsorption–desorption using a Micromeritics ASAP2010 accelerated surface area and porosimetry system (Micromeritics Co., Norcross, USA). The surface elemental compositions of the ZnO nanomaterials were determined with X-ray photoelectron spectroscopy (XPS) (PHI 5000 VersaProbe, Tokyo, Japan). The UV-vis diffuse reflectance spectra (DRS) of the ZnO nanomaterials were obtained by using a Shimadzu UV-3600 spectrophotometer equipped with an integrating sphere. Raman spectra of the ZnO nanomaterials were recorded with a Renishaw inVia Raman spectrometer (RM2000, London, UK) with an excitation wavelength of 448 nm. The photoluminescence (PL) spectra of the ZnO nanomaterials were recorded on a FLSP920 fluorescence spectrophotometer using 325 nm emission. The electron paramagnetic resonance (EPR) spectra of ZnO suspensions in water and methanol were obtained by a MS400 EPR spectrometer (Magnettech, Germany), with radicals trapped by DMPO. Thermogravimetric analysis (TGA) data were recorded at a heating rate of 10 °C min^{-1} in air with simultaneous thermogravimetry/differential thermal analyzers (TGA/DSC1, Mettler Toledo, Switzerland). Photocurrent measurements were carried out using a CHI660D (CH Instruments, Shanghai, China) electrochemistry workstation with a three-electrode system in an electrolyte solution of 0.1 M Na_2SO_4 under simulated sunlight illumination from a 500 W xenon lamp. The ZnO nanomaterials were prepared into a thin film on fluorine-doped tin oxide (FTO) glass slide to serve as the working electrode, and a platinum wire and a Ag/AgCl electrode were used as the counter and reference electrodes, respectively. Ultraviolet photoelectron spectroscopy (UPS) analysis was performed using a VG Scienta R4000 analyzer equipped with a He I light source, which has a photon energy of 21.2 eV.

2.4 Photochemical experiments

All the photochemical experiments were performed at 25 ± 1 °C, using a solar simulator (Suntest XLS+, Atlas), which is equipped with a 1700 W xenon lamp and a solar filter ($\lambda \geq$ 290 nm). The irradiance spectrum of the xenon lamp was recorded on a spectrometer (USB-4000, Ocean Optics Inc.), and for comparison, we also measured the spectrum of natural sunlight at ground level on a summer day (Fig. S2†). All the samples were placed in a specially made cylindrical quartz container (diameter 9.5 cm, height 4.5 cm, wall thickness 2 mm). In order to eliminate the pH effects, all solutions were maintained at pH 7.0 with a phosphate buffer, and the presence of the buffer has negligible effects on the photochemical formation of ROS.

Determination of steady-state concentrations of $O_2^{\bullet-}$ ($[O_2^{\bullet-}]_{ss}$). Due to the low concentration and short lifetime of $O_2^{\bullet-}$ in water, MCLA has been employed as a chemiluminescent probe, which selectively reacts with $O_2^{\bullet-}$ in a flow injection analysis (FIA) system (Waterville Analytical, Waterville, ME, USA). During the measurement, the MCLA regent, which was prepared according to the protocol of Rose and Waite,[33] and the sample were pumped into the flow cell to yield a chemiluminescent signal at 455 nm, which was detected by a photomultiplier (PMT). The calibration curve of $O_2^{\bullet-}$ concentration *versus* corresponding signal intensity is shown in Fig. S3.† To account for the $O_2^{\bullet-}$ concentration decay before the sample enters the PMT, we used a logarithm function to model the $O_2^{\bullet-}$ concentration decay profile, as previously described.[34] Details about the calculation are provided in the (ESI†).

Determination of the steady-state concentrations of $^1O_2$ and $HO^\bullet$ ($[^1O_2]_{ss}$ and $[HO^\bullet]_{ss}$). The steady-state concentrations of $^1O_2$ and $HO^\bullet$ were measured using FFA and TA as chemical probes, respectively.[35] Under our irradiated condition, direct photodegradation of TA and FFA was negligible in DI water.[36] For the determination of $^1O_2$, ZnO suspensions with FFA were irradiated under the solar simulator for 10 min, and then the FFA concentrations in the suspensions were determined by an ultrahigh performance liquid chromatograph (UHPLC) with a UV detector (λ = 219 nm) and a Gemini C18 column (4.6 × 250 mm, 5 μm). The steady-state concentration of $^1O_2$ was calculated from the temporal change of FFA concentration,[37] with calculation details provided in the ESI.†

The steady-state concentration of $HO^\bullet$ was measured by using varied concentrations of TA in ZnO suspensions, which can selectively quench the $HO^\bullet$ radicals to produce 2HTA. The concentration of 2HTA was measured using high performance liquid chromatography (HPLC) with fluorescence detection (excitation wavelength λ_{ex} = 315 nm and emission wavelength λ_{em} = 425 nm).[38] The steady-state concentration of $HO^\bullet$ was calculated based on the formation rates of 2HTA, with calculation details provided in the ESI.†

2.5 Photocatalytic degradation experiments

The photocatalytic degradation experiments of tetracycline were carried out in an XPA-system photochemical reactor (Xujiang Electromechanical Plant, Nanjing, China), using a 500 W xenon lamp with a solar filter ($\lambda \geq$ 290 nm) as the light source to provide the simulated sunlight. In a typical degradation experiment, 10 mg of ZnO powder was dispersed in 50 mL of tetracycline aqueous solution (C_0 = 30 mg L^{-1}), in the absence or presence of one of the active species scavengers: BQ, IPA, and TEOA as scavengers of $O_2^{\bullet-}$, $HO^\bullet$ and photogenerated holes (h^+), respectively. The suspensions were stirred for 1 h in the dark to reach adsorption

equilibrium, and then the reaction was started. The reaction temperature was maintained at 25 °C by circulating water. Approximately 2 mL of the suspension was withdrawn at selected time intervals and filtrated through a 0.22 μm membrane filter to remove the catalyst. The concentration of tetracycline was analyzed using a HPLC (Waters e2695) with a UV/visible detector (Waters 2489) at the wavelength of 360 nm. The column used was a symmetry-phase C18 column with a length of 150 mm and diameter of 4.6 mm. The mobile phase was acetonitrile–oxalic acid solution (15 : 85, v : v) at a flow rate of 1.0 mL min^{-1}.

2.6 Toxicity test of ZnO nanomaterials to *E. coli*

The toxicity of the two ZnO materials to *E. coli* under simulated solar light was tested by incubating *E. coli* in a ZnO suspension and subsequently measuring bacterial mortality with the plate colony-counting method. Briefly, *E. coli* bacteria were resuscitated and cultured at 37 °C and pH 7 for 12 h in a beef extract peptone medium with the following composition: 5 g L^{-1} NaCl, 5 g L^{-1} beef extract, and 3 g L^{-1} peptone. Then 10 mL of ZnO nanomaterial suspension (at 5, 10, 50, 100 and 500 mg L^{-1}) was inoculated with 100 μL of *E. coli* bacteria suspension, mixed thoroughly, and then exposed to simulated sunlight, which was provided using a 500 W xenon lamp with a solar filter ($\lambda \geq 290$ nm). After 1 h incubation, 100 μL of the mixture was sampled, diluted and plated onto agar plates, and then incubated in the dark at 37 °C for 24 h. The total number of viable bacterial colonies was counted, and the colony number of inactivated bacteria was obtained by subtracting the number of colonies on the sample plate from the average colony number on control plates (with no ZnO exposure) incubated under the same conditions. The bacterial mortality was calculated by dividing the colony number of inactivated bacteria by the average number of colonies on the control plates. Concentration of Zn^{2+} ion released from the ZnO nanomaterials under simulated sunlight irradiation was measured as follows: the ZnO *E. coli* mixture suspension was filtered using filter membrane with pore size of 0.22 μm, and zinc concentration in the filtrate was quantified using inductively coupled plasma mass spectrometry (ICP-MS) (NexION 2000, PerkinElmer, USA).

3. Results and discussion

3.1 Structural and morphological characteristics of ZnO nanomaterials with different exposed facets

The XRD spectra (Fig. 1) show that the diffraction peaks of both ZnO nanomaterials can be well indexed to hexagonal wurtzite ZnO (JCPDS No. 36-1451) structure with lattice constants of $a = b = 3.249$ Å and $c = 5.206$ Å.[39] The sharp characteristic peaks in the XRD patterns imply that the ZnO nanomaterials have high degrees of crystallization.[40] Meanwhile, no peaks of other phases were observed in the spectra, which indicates that wurtzite ZnO is the only phase in the samples.[41] However, the relative intensities of the (0002) and (10$\bar{1}$0) peaks are different between the two materials, which is consistently

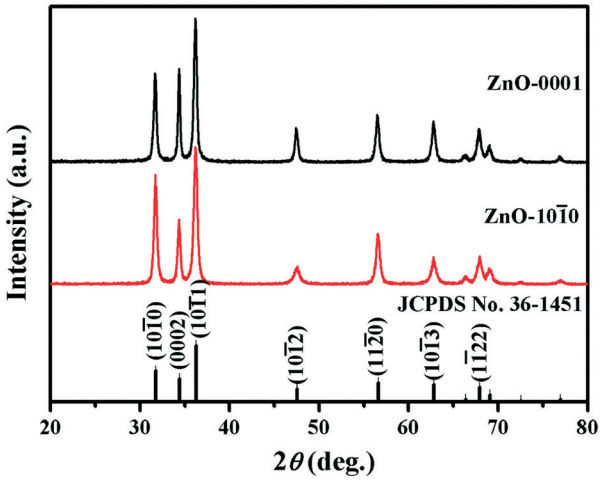

Fig. 1 XRD patterns of ZnO-0001 and ZnO-10$\bar{1}$0.

observed in repeated XRD measurements (Fig. S4†). Specifically, the diffraction intensity ratio of the (0002) plane to (10$\bar{1}$0) plane ($I_{(0002)}/I_{(10\bar{1}0)}$) of ZnO-0001 is significantly higher than that of ZnO-10$\bar{1}$0 ($p < 0.05$, $n = 3$, Student's t test) (Table S1†), implying that the exposure of the {0001} facets is more dominant in the ZnO-0001 materials.[42,43]

The morphological differences between the two ZnO nanomaterials can be seen with the SEM images (Fig. 2). Both materials display sheet-like morphology, but with distinctly different morphological details. The ZnO-0001 material shows a morphology of irregularly aggregated nanoplates, with a uniform thickness of approximately 70 nm and lateral sizes ranging from 100 to 500 nm (Fig. 2a and b). In contrast, the ZnO-10$\bar{1}$0 material shows a morphology of porous nanosheets with lateral sizes of 1–10 μm and the thickness of approximately 50 nm (Fig. 2c). It is noted that the ZnO-0001 nanoplates have smooth surface indicating high crystallinity, whereas the ZnO-10$\bar{1}$0 nanosheets contain numerous macropores larger than 50 nm, formed by the agglomeration of irregular nanoparticles (Fig. 2d). These macropores may be produced from the removal of the organic frameworks during high-temperature annealing. Due to these morphological characteristics, the specific surface area of the ZnO-10$\bar{1}$0 material is more than three times larger than that of the ZnO-0001 material (Table 1).

The structural and morphological characteristics of the two materials are confirmed by TEM (Fig. S5†). Particularly, the high-resolution TEM (HRTEM) image of a ZnO-0001 nanoplate (Fig. 2e) shows d spacing of 0.28 nm, which can be indexed to the {10$\bar{1}$0} planes of hexagonal wurtzite ZnO.[44] This suggests that the side surfaces of the nanoplates are nonpolar {10$\bar{1}$0} facets, and the top and bottom surfaces are ±{0001} facets, which grow mainly along the six symmetric directions perpendicular to the ±[10$\bar{1}$0], ±[0110], and ±[1100] crystal axes.[45] By contrast, the d spacing of the lattice fringes for ZnO-10$\bar{1}$0 is 0.26 nm (Fig. 2f), corresponding to the {0001} crystal planes of hexagonal wurtzite ZnO.[46] Thus, we conclude that the two ZnO nanomaterials have different exposed facets, as illustrated in Fig. S6.†

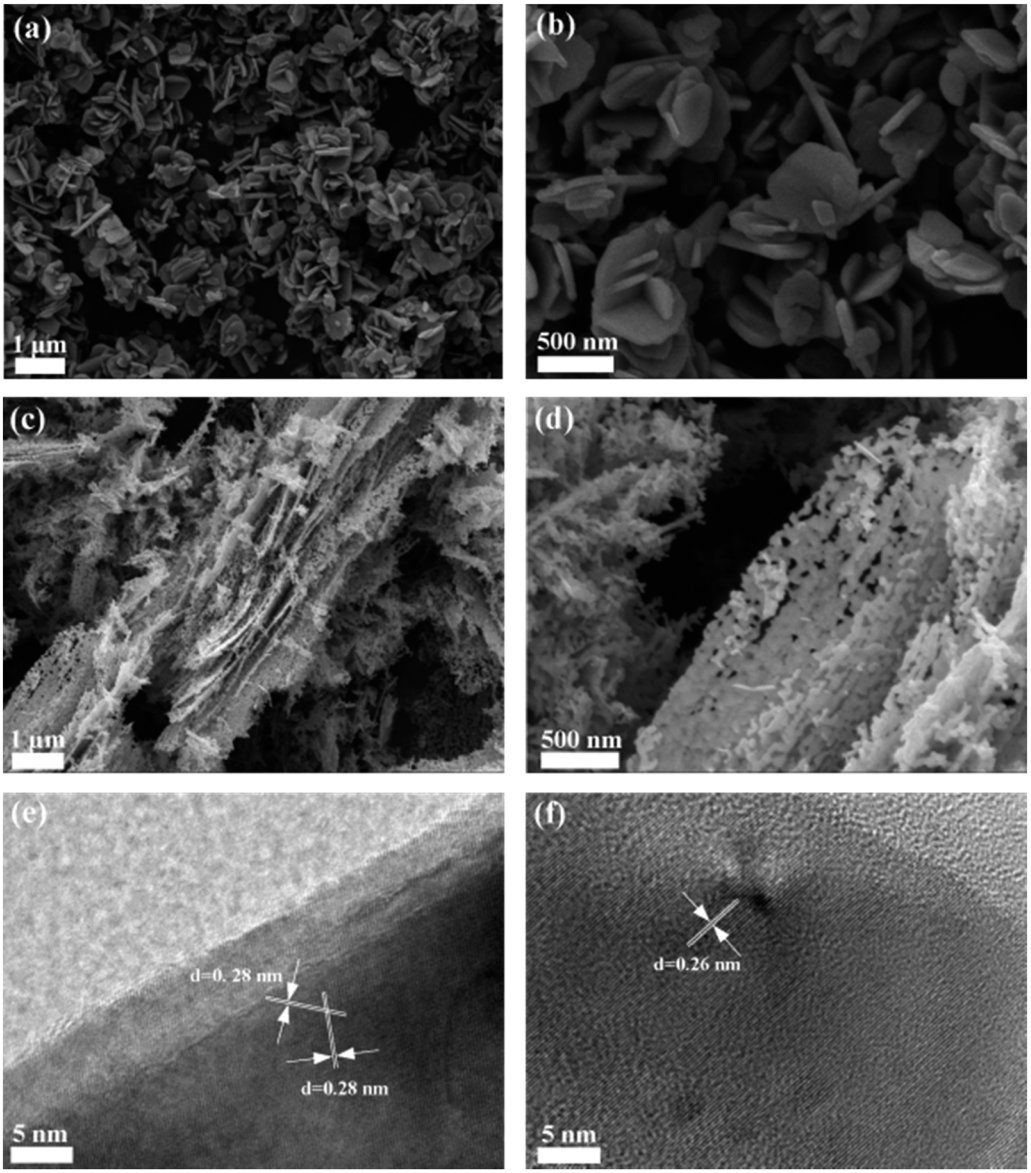

Fig. 2 SEM images of ZnO nanomaterials: ZnO-0001 with (a) low and (b) high magnification, ZnO-10$\bar{1}$0 with (c) low and (d) high magnification. HRTEM images of (e) ZnO-0001 and (f) ZnO-10$\bar{1}$0.

3.2 Facet-dependent photochemical properties of ZnO nanomaterials

The photochemical properties of the two ZnO nanomaterials were examined regarding their ability to generate ROS in aqueous solution (pH 7.0) under simulated solar irradiation (Fig. 3). The $O_2^{\bullet-}$-generating abilities of the two ZnO nanomaterials are distinctly different, as the $[O_2^{\bullet-}]_{ss}$ for ZnO-0001 (49.4 nM) was nearly four times as high as that for ZnO-10$\bar{1}$0 (12.8 nM) (Fig. 3a and Table 2), despite the much smaller SA_{BET} of the ZnO-0001 material (Table 1). By contrast, the steady-state concentrations of both $^1O_2$ and HO$^{\bullet}$ were similar between ZnO-0001 and ZnO-10$\bar{1}$0 (Fig. 3b and c and Table 2). The ROS-generating properties of the ZnO nanomaterials under simulated solar irradiation were further examined by DMPO-assisted EPR measurement (Fig. 4). The typical signal of the DMPO–$O_2^{\bullet-}$ adduct[31] was detected in the methanolic suspensions of the two ZnO nanomaterials, and the signal was much higher for ZnO-0001 than for ZnO-10$\bar{1}$0 (Fig. 4a), which confirmed that ZnO-0001 was capable to produce more $O_2^{\bullet-}$ than ZnO-10$\bar{1}$0 under identical solar irradiation. In

Table 1 Selected physicochemical properties of ZnO nanomaterials

Material	Dominant exposed facets	SA_{BET}[a] ($m^2\ g^{-1}$)	O 1s[b] (at%)		
			O_I	O_II	O_III
ZnO-0001	{0001}	10.0	72.5	27.5	0
ZnO-10$\bar{1}$0	{10$\bar{1}$0}	33.5	67.1	19.8	13.1

[a] Specific surface area measured using the Brunauer–Emmett–Teller (BET) method. [b] Surface O composition analyzed with X-ray photoelectron spectroscopy.

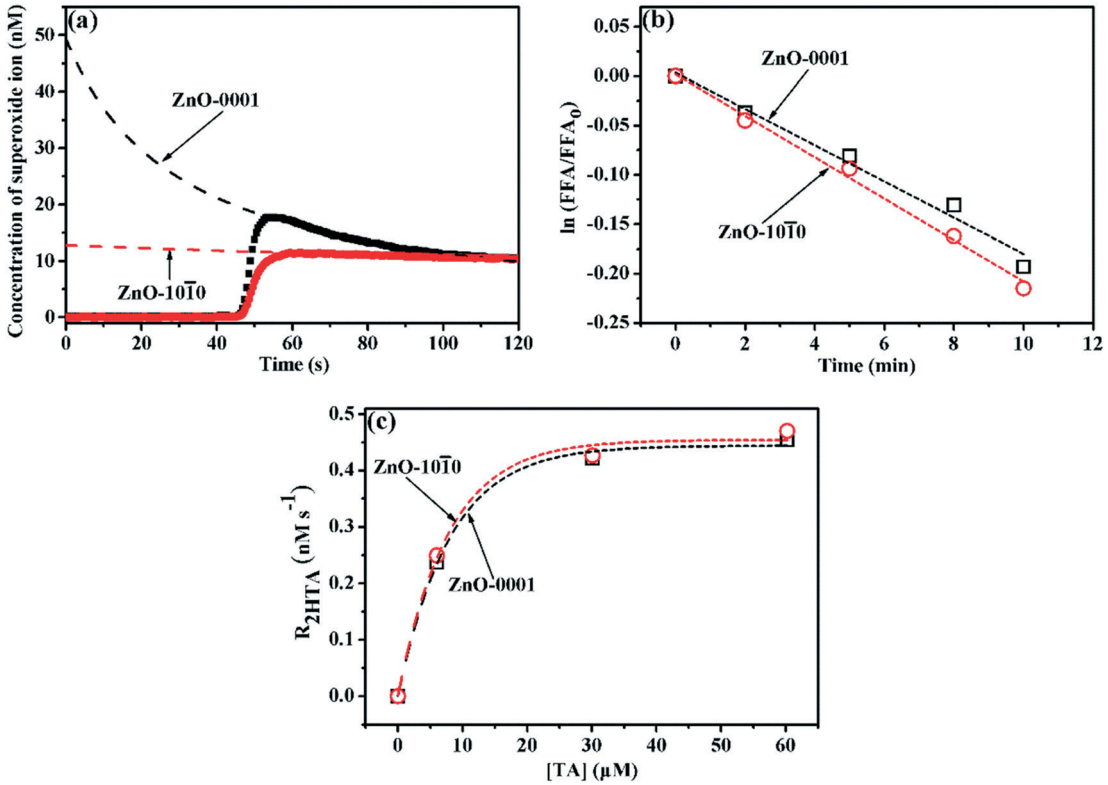

Fig. 3 Measurement of steady-state concentrations of ROS species generated by the two ZnO nanomaterials in aqueous solution under the simulated solar irradiation: (a) superoxide radical anions ($O_2^{\bullet-}$); (b) singlet oxygen ($^1O_2$), *via* the degradation of FFA; (c) hydroxyl radicals (HO$^\bullet$), *via* the formation of 2HTA.

comparison, the characteristic EPR signals of the DMPO–HO$^\bullet$ adduct[31,47] with similar intensities were observed in aqueous suspensions of both ZnO-0001 and ZnO-10$\bar{1}$0 (Fig. 4b). Thus, the qualitative EPR results are consistent with the above-mentioned quantitative analyses (Fig. 3 and Table 2).

3.3 Mechanisms controlling facet-dependent photochemical properties of ZnO nanomaterials

As discussed above, the two ZnO nanomaterials exhibit different capabilities to generate ROS (especially $O_2^{\bullet-}$) under simulated solar irradiation, even after the difference in specific surface area was taken into account, which implies that other factors determine the photochemical properties of the two ZnO nanomaterials with different exposed facets. It is well established that in semiconductor photocatalysis the $O_2^{\bullet-}$ is generated from O_2 reduction by the photogenerated electrons (e^-) at the conduction band (CB) of the semiconductor. Thus, the amount of photocatalytically generated $O_2^{\bullet-}$ can be influenced by several factors: (1) the adsorption of O_2 on the semiconductor surface, (2) the amount of CB electrons that can reach the surface of the semiconductor materials, and (3) the CB level of the semiconductor, which determines the thermodynamic driving force for the O_2 reduction reaction.[48]

Table 2 Steady-state concentrations (in nM) of ROS species produced by different ZnO nanomaterials in aqueous suspension under simulated solar irradiation

Material	$O_2^{\bullet-}$	HO$^\bullet$	$^1O_2$
ZnO-0001	49.4	4.5×10^{-4}	2.7×10^{-3}
ZnO-10$\bar{1}$0	12.8	4.7×10^{-4}	2.9×10^{-3}

We first examined the O_2 adsorption abilities of the ZnO nanomaterials. The surface chemical compositions of the ZnO nanomaterials were analyzed by XPS (Fig. S7†). The O 1s peak (Fig. S7b†) was deconvoluted to determine the relative contents of different surface oxygen species. The peak at approximately 530.2 eV (O_I) is related to oxygen in the ZnO crystal lattice (*i.e.*, the Zn–O bond), the one at about 531.4 eV (O_II) to surface chemisorbed oxygen species (O^-, O_2^- or O^{2-}) or surface hydroxyl group, and that at approximately 532.5 eV (O_III) to adsorbed H_2O molecules.[49,50] As summarized in Table 1, the relative percentage of the O_II component is higher for ZnO-0001 (27.5%) than for ZnO-10$\bar{1}$0 (19.8%), indicating that the surface of ZnO-0001 may contain more chemisorbed oxygen or OH groups. In addition, the ZnO-0001 surface has negligible content of adsorbed H_2O compared with ZnO-10$\bar{1}$0.

The difference in O_2 adsorption abilities manifested by the XPS results were corroborated with TGA analysis of the ZnO nanomaterials (Fig. S8†). According to Mueller *et al.*,[51] the weight loss in the 30–120 °C range is due to the loss of physically adsorbed water, and those in the 120–300 °C and 300–600 °C ranges are related to weakly and strongly bonded

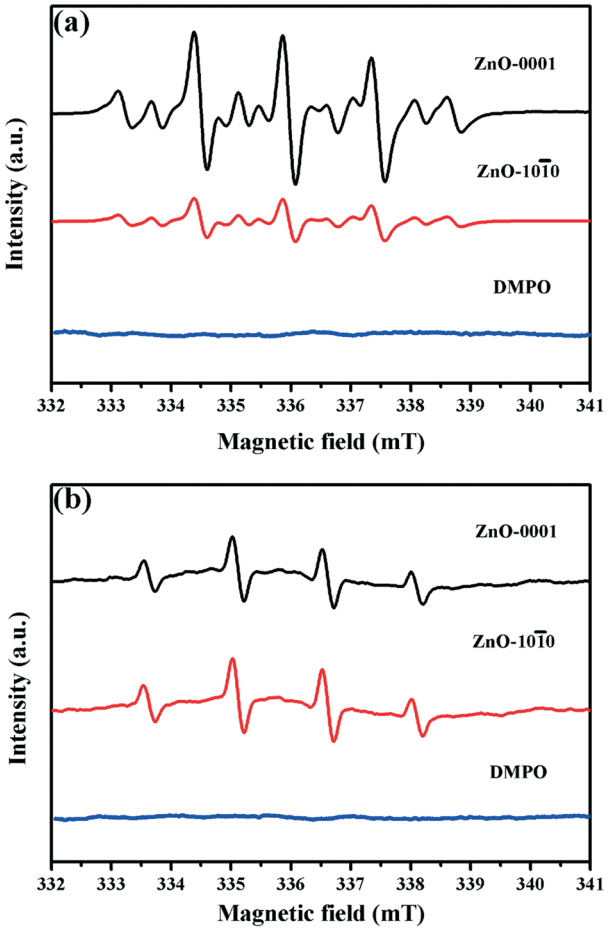

Fig. 4 EPR spectra of the ZnO nanomaterials (1.2×10^{-2} mol L^{-1}) and DMPO (0.25 mol L^{-1}) in (a) methanolic and (b) aqueous suspensions after irradiation by simulated solar light.

OH groups, respectively. Compared with ZnO-0001, ZnO-10$\bar{1}$0 contains significantly more adsorbed H_2O and OH groups ($p < 0.01$, $n = 3$, Student's t test) (Table 3). It should be noted that although TGA is a bulk analysis technique, all the OH groups are supposed to be present on the surface of the ZnO nanomaterials. Thus, the XPS and TGA data together indicate that ZnO-0001 has higher adsorption affinity towards O_2 than ZnO-10$\bar{1}$0.

This discrepancy in O_2 adsorption between the materials is most likely due to the difference in the surface atomic structures of their predominant exposed facets. The Zn atoms on the {0001} facets are usually coordinatively unsaturated with more dangling bonds, and thus the adsorption of O_2 is more likely to occur on the {0001} facets than on the {10$\bar{1}$0} facets.[43] In addition, the chemisorption energy values of O_2 molecules on the {0001} and {10$\bar{1}$0} facets are −1.0665 eV and −0.5233 eV, respectively.[52] The more negative the chemisorption energy, the stronger the ability to adsorb O_2.[52] Therefore, this previous theoretical calculation result is in accordance with our finding that the ZnO-0001 material with predominantly exposed {0001} facets has higher O_2 adsorption affinity than the ZnO-10$\bar{1}$0 material with predominantly exposed {10$\bar{1}$0} facets.

Secondly, the amount of CB electrons produced by the two ZnO nanomaterials were compared by examining their light absorption and charge separation efficiencies. Based on the UV-vis DRS spectra (Fig. 5a) and the corresponding Tauc plots (Fig. 5b), ZnO-10$\bar{1}$0 has a narrower band gap (E_g, 2.95 eV) than ZnO-0001 (3.11 eV). Thus, ZnO-10$\bar{1}$0 has stronger light absorption capability and can generate more CB electrons than ZnO-0001 under identical light irradiation conditions. Moreover, it is noted that the ZnO-10$\bar{1}$0 material has absorption in the visible-light range ($\lambda \geq 400$ nm), likely because of the more abundant defects in ZnO-10$\bar{1}$0,[53] as evidenced from the XPS (Fig. S7c†) and Raman spectroscopy

Table 3 Weight percentages (w/w, %) of adsorbed H_2O and OH groups calculated from TGA results (ZnO-0001 and ZnO-10$\bar{1}$0 showed significant difference (mean ± SD, $n = 3$, $p < 0.01$) in total OH content, by Student's t test)

Material	H_2O	OH_{weak}	OH_{strong}	OH_{total}
ZnO-0001	0.15 ± 0.01	0.40 ± 0.03	0.82 ± 0.06	1.22 ± 0.09
ZnO-10$\bar{1}$0	1.23 ± 0.08	1.73 ± 0.12	1.41 ± 0.01	3.14 ± 0.13

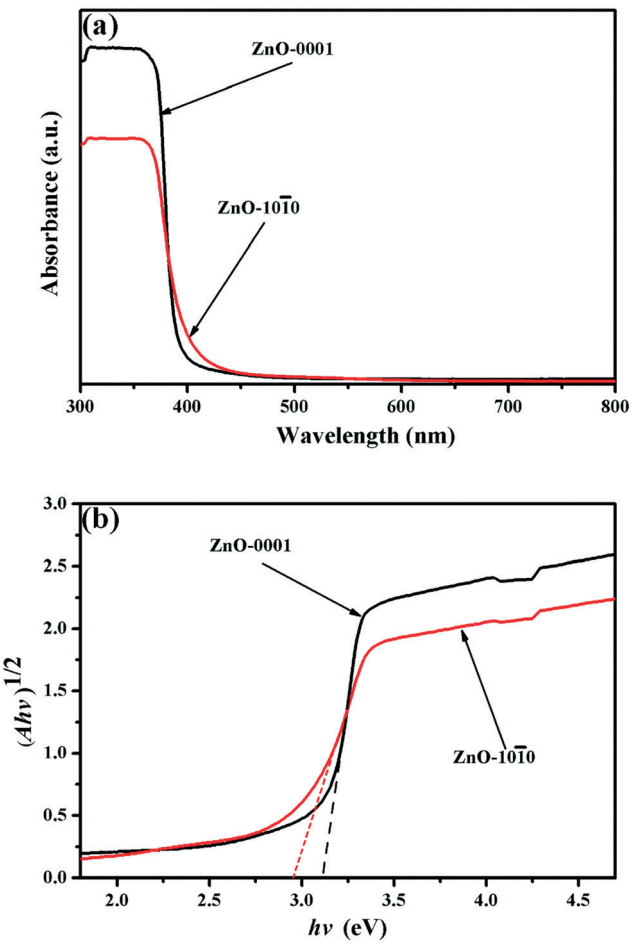

Fig. 5 (a) UV-vis DRS spectra and (b) plots of $(Ahv)^{1/2}$ *versus* photon energy (hv) of ZnO-0001 and ZnO-10$\bar{1}$0.

(Fig. S9†) analyses (the assignment of Raman bands is provided in the ESI†). On the other hand, ZnO-0001 has stronger fluorescence signal in the PL spectrum than ZnO-10$\bar{1}$0 (Fig. 6a), suggesting higher recombination rates of photogenerated e^- and h^+ and accordingly lower separation efficiency of the charge carriers. This is further supported by the lower photocurrent density of the ZnO-0001 material (Fig. 6b). Thus, considering the generation and recombination dynamics of charge carriers, we concluded that the ZnO-0001 material is indeed inferior to the ZnO-10$\bar{1}$0 material in providing CB electrons for the reduction of surface adsorbed O_2 to produce $O_2^{\bullet-}$ radical.

Note that the efficiencies of reduction and oxidation reactions on the surface of photoexcited semiconductor nanoparticles depend not only on the amount of CB electrons or VB holes that can reach the surface of a nanomaterial, but also on the CB and VB positions of the semiconductor, which determine the thermodynamic driving force of the surface redox reactions. The level of the VB maximum (E_{VBM}) was measured from UPS analysis (Fig. S10†), which, in combination with the E_g values, was then used to determine the CB minimum level (E_{CBM}) of the materials (Fig. S11†), where $E_{CBM} = E_{VBM} - E_g$. The calculated E_{VBM} energies of ZnO-0001 and ZnO-10$\bar{1}$0 are 3.3 and 3.25 eV, respectively, relative to the Fermi level, which are equivalent to 7.25 and 7.28 eV relative to the vacuum level (Fig. S11†). These E_{VBM} energies correspond to 2.75 and 2.78 eV relative to the normal hydrogen electrode (NHE) level, since the scale factor relating the NHE-based redox potential to the energy levels on the absolute vacuum energy scale is −4.5 eV.[54] Thus, the corresponding E_{CBM} potentials are −0.36 and −0.17 eV *vs.* NHE. The more negative CB potential of ZnO-0001 can provide greater thermodynamic driving force for the surface O_2 reduction reaction than for ZnO-10$\bar{1}$0 (Fig. 7). Therefore, even though ZnO-0001 is not as effective in generating CB electrons as ZnO-10$\bar{1}$0, the greater thermodynamic driving force associated with this material still results in greater capability for the reduction of adsorbed O_2 to $O_2^{\bullet-}$.

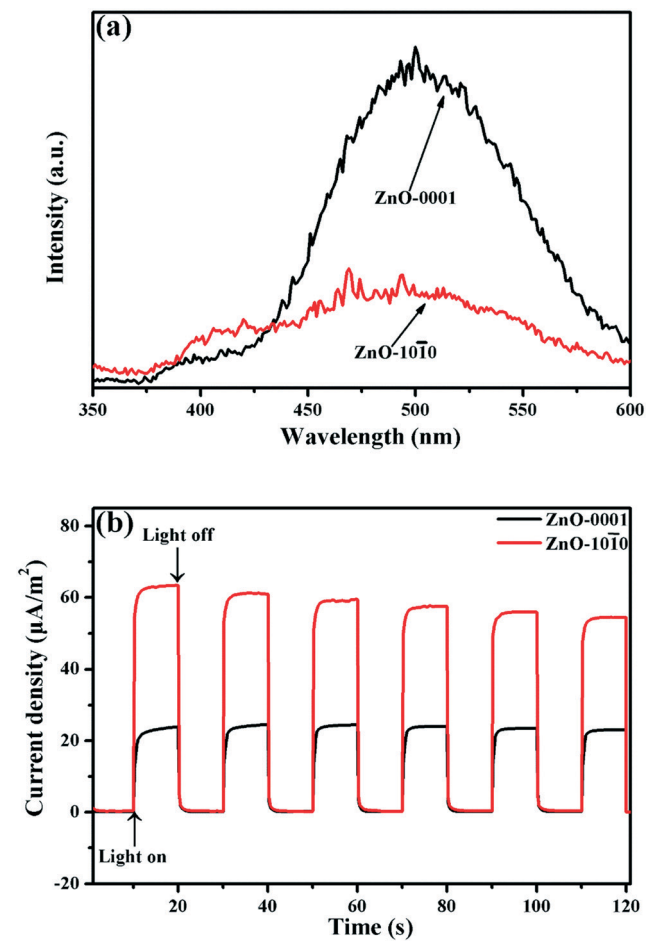

Fig. 6 (a) PL spectra and (b) photocurrent response of the ZnO nanomaterials under simulated solar irradiation.

3.4 Environmental implications

Even though $O_2^{\bullet-}$ is a weak oxidant compared to $HO^{\bullet}$ and $^1O_2$, it can play an important role in certain (photo)chemical and biological processes, given that it can occur at much higher concentrations than $HO^{\bullet}$ (*e.g.*, in this study) and that it can participate in various types of reactions, even serving as a precursor to H_2O_2, which further results in $HO^{\bullet}$ generation.[55] The important role of $O_2^{\bullet-}$ has been observed in both photocatalytic applications of semiconductor nanomaterials and their environmental behaviors and impacts from a life-cycle perspective. For instance, $O_2^{\bullet-}$ was identified as the primary oxidant for the photocatalytic oxidation of arsenic(III) over TiO_2 nanomaterials with different exposed facets.[30] The facet-dependent formation of $O_2^{\bullet-}$ was also a major cause for the enhanced photocatalytic formaldehyde oxidation by $SrTiO_3$ nanocrystals.[29] Moreover, the diverse ecotoxicological effects of metal oxide nanomaterials have been attributed to their different capabilities to generate $O_2^{\bullet-}$ under light illumination.[20] Herein, the potential implications of facet-dependent $O_2^{\bullet-}$ generation of the two ZnO nanomaterials in engineered or natural aquatic environments are illustrated by

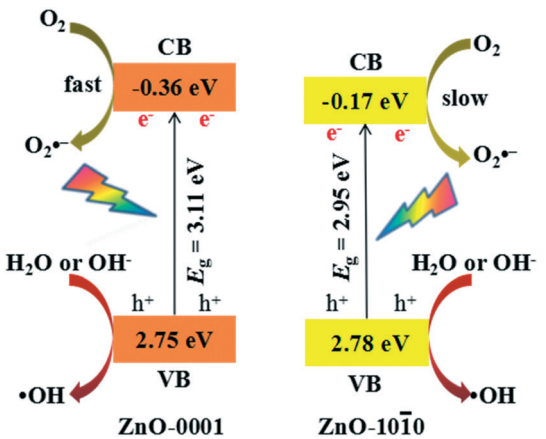

Fig. 7 Scheme of the band structures of ZnO-0001 and ZnO-10$\bar{1}$0, in which the conduction band (CB) positions determine the thermodynamic driving force for surface O_2 reduction reactions.

evaluating their performance in photocatalytic degradation of tetracycline and inactivation of *E. coli*.

Overall, ZnO-0001 was more effective than ZnO-10$\bar{1}$0 in photocatalytic degradation of tetracycline, resulting in faster removal of tetracycline in the aqueous suspension (Fig. S12†). The roles of different reactive species (*i.e.*, $O_2^{\bullet-}$, $HO^{\bullet}$ and h^+) were examined by radical quenching experiments (Fig. 8). Interestingly, in the presence of BQ (a $O_2^{\bullet-}$ scavenger), tetracycline degradation with ZnO-0001 decreased to a much greater extent (by 37%) than with ZnO-10$\bar{1}$0 (by 14%). This observation indicated that the $O_2^{\bullet-}$ radical plays an important role in the photocatalytic degradation of tetracycline, and the relative extent of the decrease in tetracycline removal efficiency is consistent with the $O_2^{\bullet-}$ concentration generated by the two ZnO materials (Table 2). The addition of IPA (a $HO^{\bullet}$ scavenger) only slightly decreased the tetracycline removal efficiency for both ZnO materials, suggesting that $HO^{\bullet}$ plays a minor role in the photocatalytic degradation of tetracycline. When TEOA was added as a scavenger of h^+, tetracycline removal decreased by 15% and 36%, respectively, with ZnO-0001 and ZnO-10$\bar{1}$0, further indicating that the greater photocatalytic efficiency of ZnO-0001 is attributable to its greater $O_2^{\bullet-}$ generation capability (the greater contribution of h^+ to tetracycline degradation with ZnO-10$\bar{1}$0 is consistent with the higher light absorption and charge separation efficiencies of this material as shown in Fig. 5 and 6). Overall, these results demonstrated that the facet-dependent ROS generation significantly determines the overall photocatalytic oxidation efficiency of ZnO nanomaterials and consequently, can influence both application and implication of these nanomaterials in terms of interaction with organic contaminants.

The relative toxicity of the two ZnO nanomaterials to *E. coli* under simulated solar light is shown in Fig. 9. ZnO-0001 was markedly more effective in inactivating *E. coli* than ZnO-10$\bar{1}$0. For instance, 68% inactivation of *E. coli* cells was achieved with ZnO-0001 upon irradiation under simulated sunlight for 1 h at a ZnO dose of 10 mg L^{-1}, whereas the inactivation efficiency was only 40% for ZnO-10$\bar{1}$0 under the same conditions. The toxicity of ZnO nanomaterials to bacteria including *E. coli* can usually be attributed to dissolution and release of Zn^{2+} and/or to the generation and action of ROS.[56,57] Hence, the concentrations of Zn^{2+} ion released from the ZnO nanomaterials (tested at 10 mg L^{-1} and 100 mg L^{-1} ZnO) under simulated sunlight irradiation were measured. Interestingly, ZnO-0001 released less Zn^{2+} ions than ZnO-10$\bar{1}$0 (Fig. S13†). Thus, dissolution and release of Zn^{2+} can be ruled out as a main cause of the higher bacterial toxicity of ZnO-0001. Instead, higher generation rate of ROS, $O_2^{\bullet-}$ in particular, is most likely the reason for the higher toxicity of ZnO-0001, which is consistent with the toxicity mechanism of ZnO nanomaterials to *Photobacterium phosphoreum* bacterium.[20]

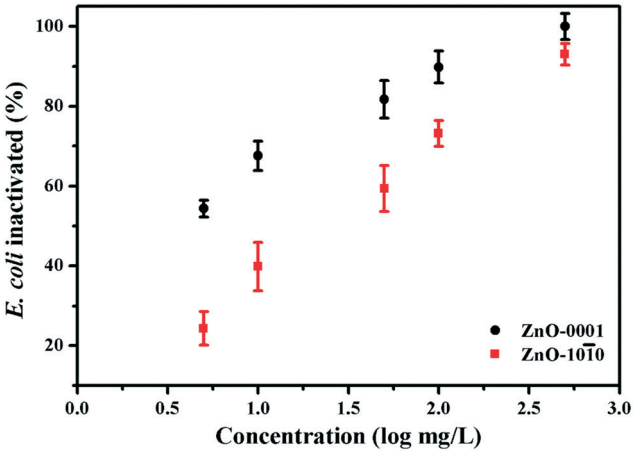

Fig. 9 Antibacterial activity of ZnO-0001 and ZnO-10$\bar{1}$0 nanomaterials under simulated solar irradiation. Error bars represent ± one standard deviation from the mean (n = 3).

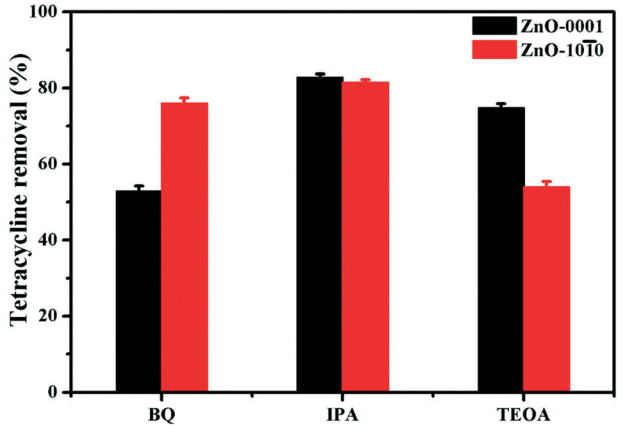

Fig. 8 Photodegradation of tetracycline by ZnO-0001 or ZnO-10$\bar{1}$0 in aqueous solutions with or without radical scavengers, after irradiation under simulated solar for 3 h. The 1,4-benzoquinone (BQ), isopropyl alcohol (IPA), triethanolamine (TEOA) were used as scavengers of $O_2^{\bullet-}$, $HO^{\bullet}$ and h^+, respectively. Error bars represent ± one standard deviation from the mean (n = 3).

4. Conclusions

A ZnO nanoplate material with predominantly exposed {0001} facets and a nanosheet material with predominantly exposed {10$\bar{1}$0} facets exhibit different photochemical properties in terms of ROS generation under simulated solar irradiation. The ZnO nanoplates with predominantly exposed {0001} facets can generate more $O_2^{\bullet-}$ radical as compared to the porous ZnO nanosheets with predominantly exposed {10$\bar{1}$0} facets. The exposed {0001} facets of ZnO have more unsaturated zinc atoms, which is conducive to the adsorption of O_2, than the {10$\bar{1}$0} facets. Although the ZnO-10$\bar{1}$0 material can provide more CB electrons due to its higher light absorption and charge separation efficiencies, its CB level is lower than that of the ZnO-0001 material, thus limiting the thermodynamic driving force for the reduction of adsorbed O_2 to $O_2^{\bullet-}$. In summary, this study further demonstrates that the photochemical properties of metal oxide semiconductor nanomaterials such as ZnO are greatly affected by exposed facets, which determine the abundance of unsaturated

surface atoms as well as the band structures. Therefore, exposed facet is an essential parameter for predicting the photocatalytic activity and environmental implications of semiconductor nanomaterials.

Conflicts of interest

The authors declare no conflict of interest.

Acknowledgements

This project was supported by the National Science Fund for Distinguished Young Scholars (Grant 21425729), the Ministry of Science and Technology of China (Grant 2014CB932001), the Fundamental Research Funds for the Central Universities and the 111 Program of Ministry of Education of China (T2017002).

References

1 A. A. Keller and A. Lazareva, Predicted releases of engineered nanomaterials: from global to regional to local, *Environ. Sci. Technol. Lett.*, 2014, **1**, 65–70.
2 T. Y. Sun, D. M. Mitrano, N. A. Bornhoft, M. Scheringer, K. Hungerbuhler and B. Nowack, Envisioning nano release dynamics in a changing world: using dynamic probabilistic modeling to assess future environmental emissions of engineered nanomaterials, *Environ. Sci. Technol.*, 2017, **51**, 2854–2863.
3 X. He, W. G. Aker, P. P. Fu and H.-M. Hwang, Toxicity of engineered metal oxide nanomaterials mediated by nano-bio-eco-interactions: a review and perspective, *Environ. Sci.: Nano*, 2015, **2**, 564–582.
4 V. L. Colvin, The potential environmental impact of engineered nanomaterials, *Nat. Biotechnol.*, 2003, **21**, 1166–1170.
5 M. R. Wiesner, G. V. Lowry, P. Alvarez, D. Dionysiou and P. Biswas, Assessing the risks of manufactured nanomaterials, *Environ. Sci. Technol.*, 2006, **40**, 4336–4345.
6 C. O. Hendren, G. V. Lowry, J. M. Unrine and M. R. Wiesner, A functional assay-based strategy for nanomaterial risk forecasting, *Sci. Total Environ.*, 2015, **536**, 1029–1037.
7 R. S. Lankone, K. E. Challis, Y. Bi, D. Hanigan, R. B. Reed, T. Zaikova, J. E. Hutchison, P. Westerhoff, J. Ranville, H. Fairbrother and L. M. Gilbertson, Methodology for quantifying engineered nanomaterial release from diverse product matrices under outdoor weathering conditions and implications for life cycle assessment, *Environ. Sci.: Nano*, 2017, **4**, 1784–1797.
8 C. M. Wilke, J.-F. Gaillard and K. A. Gray, The critical role of light in moderating microbial stress due to mixtures of engineered nanomaterials, *Environ. Sci.: Nano*, 2018, **5**, 96–102.
9 V. Sogne, F. Meier, T. Klein and C. Contado, Investigation of zinc oxide particles in cosmetic products by means of centrifugal and asymmetrical flow field-flow fractionation, *J. Chromatogr. A*, 2017, **1515**, 196–208.
10 P. J. Perez Espitia, N. D. F. Ferreira Soares, J. S. dos Reis Coimbra, N. J. de Andrade, R. S. Cruz and E. A. Alves Medeiros, Zinc oxide nanoparticles: synthesis, antimicrobial activity and food packaging applications, *Food Bioprocess Technol.*, 2012, **5**, 1447–1464.
11 D. J. Gargas, M. C. Moore, A. Ni, S.-W. Chang, Z. Zhang, S.-L. Chuang and P. Yang, Whispering gallery mode lasing from zinc oxide hexagonal nanodisks, *ACS Nano*, 2010, **4**, 3270–3276.
12 J. R. Rangel-Mendez, J. Matos, L. F. Chazaro-Ruiz, A. C. Gonzalez-Castillo and G. Barrios-Yanez, Microwave-assisted synthesis of C-doped TiO_2 and ZnO hybrid nanostructured materials as quantum-dots sensitized solar cells, *Appl. Surf. Sci.*, 2018, **434**, 744–755.
13 Y. Li, Z. Celik-Butler and D. P. Butler, An integrated piezoelectric zinc oxide nanowire micro-energy harvester, *Nano Energy*, 2016, **26**, 456–465.
14 R. Tabassum and B. D. Gupta, Simultaneous tuning of electric field intensity and structural properties of ZnO: graphene nanostructures for FOSPR based nicotine sensor, *Biosens. Bioelectron.*, 2017, **91**, 762–769.
15 C.-C. Chuang, A. Prasannan, B.-R. Huang, P.-D. Hong and M.-Y. Chiang, Simple synthesis of eco-friendly multifunctional silk-sericin capped zinc oxide nanorods and their potential for fabrication of hydrogen sensors and UV photodetectors, *ACS Sustainable Chem. Eng.*, 2017, **5**, 4002–4010.
16 S. Sakthivel, B. Neppolian, M. V. Shankar, B. Arabindoo, M. Palanichamy and V. Murugesan, Solar photocatalytic degradation of azo dye: comparison of photocatalytic efficiency of ZnO and TiO_2, *Sol. Energy Mater. Sol. Cells*, 2003, **77**, 65–82.
17 N. Daneshvar, D. Salari and A. R. Khataee, Photocatalytic degradation of azo dye acid red 14 in water on ZnO as an alternative catalyst to TiO_2, *J. Photochem. Photobiol., A*, 2004, **162**, 317–322.
18 S. Wang, P. Kuang, B. Cheng, J. Yu and C. Jiang, ZnO hierarchical microsphere for enhanced photocatalytic activity, *J. Alloys Compd.*, 2018, **741**, 622–632.
19 N. B. Saleh, D. J. Milliron, N. Aich, L. E. Katz, H. M. Liljestrand and M. J. Kirisits, Importance of doping, dopant distribution, and defects on electronic band structure alteration of metal oxide nanoparticles: implications for reactive oxygen species, *Sci. Total Environ.*, 2016, **568**, 926–932.
20 D. Wang, L. Zhao, H. Ma, H. Zhang and L.-H. Guo, Quantitative analysis of reactive oxygen species photogenerated on metal oxide nanoparticles and their bacteria toxicity: the role of superoxide radicals, *Environ. Sci. Technol.*, 2017, **51**, 10137–10145.
21 T. Daimon, T. Hirakawa, M. Kitazawa, J. Suetake and Y. Nosaka, Formation of singlet molecular oxygen associated with the formation of superoxide radicals in aqueous suspensions of TiO_2 photocatalysts, *Appl. Catal., A*, 2008, **340**, 169–175.
22 H. Lu, W. Fan, H. Dong and L. Liu, Dependence of the irradiation conditions and crystalline phases of TiO_2

nanoparticles on their toxicity to *Daphnia magna*, *Environ. Sci.: Nano*, 2017, **4**, 406–414.

23 L. Shi, S. Zhuo, M. Abulikemu, G. Mettela, T. Palaniselvam, S. Rasul, B. Tang, B. Yan, N. B. Saleh and P. Wang, Annealing temperature effects on photoelectrochemical performance of bismuthvanadate thin film photoelectrodes, *RSC Adv.*, 2018, **8**, 29179–29188.

24 X. Xu, X. Duan, Z. Yi, Z. Zhou, X. Fan and Y. Wang, Photocatalytic production of superoxide ion in the aqueous suspensions of two kinds of ZnO under simulated solar light, *Catal. Commun.*, 2010, **12**, 169–172.

25 D. Jiang, W. Wang, L. Zhang, Y. Zheng and Z. Wang, Insights into the surface-defect dependence of photoreactivity over CeO_2 nanocrystals with well-defined crystal facets, *ACS Catal.*, 2015, **5**, 4851–4858.

26 K. S. Ranjith and R. T. R. Kumar, Surfactant free, simple, morphological and defect engineered ZnO nanocatalyst: effective study on sunlight driven and reusable photocatalytic properties, *J. Photochem. Photobiol., A*, 2016, **329**, 35–45.

27 N. Liu, Y. Chang, Y. Feng, Y. Cheng, X. Sun, H. Jian, Y. Feng, X. Li and H. Zhang, {101}-{001} Surface heterojunction-enhanced antibacterial activity of titanium dioxide nanocrystals under sunlight irradiation, *ACS Appl. Mater. Interfaces*, 2017, **9**, 5907–5915.

28 M.-S. Hsieh, H.-J. Su, P.-L. Hsieh, Y.-W. Chiang and M. H. Huang, Synthesis of Ag_3PO_4 crystals with tunable shapes for facet-dependent optical property, photocatalytic activity, and electrical conductivity examinations, *ACS Appl. Mater. Interfaces*, 2017, **9**, 39086–39093.

29 X. Wu, X. Wang, J. Li and G. Zhang, Boosting molecular oxygen activation of $SrTiO_3$ by engineering exposed facets for highly efficient photocatalytic oxidation, *J. Mater. Chem. A*, 2017, **5**, 23822–23830.

30 L. Yan, J. Du and C. Jing, How TiO_2 facets determine arsenic adsorption and photooxidation: spectroscopic and DFT studies, *Catal. Sci. Technol.*, 2016, **6**, 2419–2426.

31 M. L. Pan, H. J. Zhang, G. D. Gao, L. Liu and W. Chen, Facet-dependent catalytic activity of nanosheet-assembled bismuth oxyiodide microspheres in degradation of bisphenol A, *Environ. Sci. Technol.*, 2015, **49**, 6240–6248.

32 H. Xu, W. J. Cooper, J. Jung and W. Song, Photosensitized degradation of amoxicillin in natural organic matter isolate solutions, *Water Res.*, 2011, **45**, 632–638.

33 A. L. Rose and D. Waite, Role of superoxide in the photochemical reduction of iron in seawater, *Geochim. Cosmochim. Acta*, 2006, **70**, 3869–3882.

34 A. L. Rose, J. W. Moffett and T. D. Waite, Determination of superoxide in seawater using 2-methyl-6-(4-methoxyphenyl)-3,7-dihydroimidazo 1,2-a pyrazin-3(7H)-one chemiluminescence, *Anal. Chem.*, 2008, **80**, 1215–1227.

35 J. M. Burns, W. J. Cooper, J. L. Ferry, D. W. King, B. P. DiMento, K. McNeill, C. J. Miller, W. L. Miller, B. M. Peake, S. A. Rusak, A. L. Rose and T. D. Waite, Methods for reactive oxygen species (ROS) detection in aqueous environments, *Aquat. Sci.*, 2012, **74**, 683–734.

36 L. Yin, H. Zhou, L. Lian, S. Yan and W. Song, Effects of C_{60} on the photochemical formation of reactive oxygen species from natural organic matter, *Environ. Sci. Technol.*, 2016, **50**, 11742–11751.

37 E. Appiani, R. Ossola, D. E. Latch, P. R. Erickson and K. McNeill, Aqueous singlet oxygen reaction kinetics of furfuryl alcohol: effect of temperature, pH, and salt content, *Environ. Sci.: Processes Impacts*, 2017, **19**, 507–516.

38 A. Samuni, S. Goldstein, A. Russo, J. B. Mitchell, M. C. Krishna and P. Neta, Kinetics and mechanism of hydroxyl radical and OH-adduct radical reactions with nitroxides and with their hydroxylamines, *J. Am. Chem. Soc.*, 2002, **124**, 8719–8724.

39 S.-M. Li, L.-X. Zhang, M.-Y. Zhu, G.-J. Ji, L.-X. Zhao, J. Yin and L.-J. Bie, Acetone sensing of ZnO nanosheets synthesized using room-temperature precipitation, *Sens. Actuators, B*, 2017, **249**, 611–623.

40 R. Krishnapriya, S. Praneetha, S. Kannan and A. V. Murugan, Unveiling the Co^{2+} ion doping-induced hierarchical shape evolution of ZnO: in correlation with magnetic and photovoltaic performance, *ACS Sustainable Chem. Eng.*, 2017, **5**, 9981–9992.

41 S. S. Mali, H. Kim, W. Y. Jang, H. S. Park, P. S. Patil and C. K. Hong, Novel synthesis and characterization of mesoporous ZnO nanofibers by electrospinning technique, *ACS Sustainable Chem. Eng.*, 2013, **1**, 1207–1213.

42 S. Tian, F. Yang, D. Zeng and C. Xie, Solution-processed gas sensors based on ZnO nanorods array with an exposed (0001) facet for enhanced gas-sensing properties, *J. Phys. Chem. C*, 2012, **116**, 10586–10591.

43 N. Qin, Q. Xiang, H. Zhao, J. Zhang and J. Xu, Evolution of ZnO microstructures from hexagonal disk to prismoid, prism and pyramid and their crystal facet-dependent gas sensing properties, *CrystEngComm*, 2014, **16**, 7062–7073.

44 M. Huang, S. Weng, B. Wang, J. Hu, X. Fu and P. Liu, Various facet tunable ZnO crystals by a scalable solvothermal synthesis and their facet-dependent photocatalytic activities, *J. Phys. Chem. C*, 2014, **118**, 25434–25440.

45 Q. Zhao, Q. Shen, F. Yang, H. Zhao, B. Liu, Q. Liang, A. Wei, H. Yang and S. Liu, Direct growth of ZnO nanodisk networks with an exposed (0001) facet on Au comb-shaped interdigitating electrodes and the enhanced gas-sensing property of polar {0001} surfaces, *Sens. Actuators, B*, 2014, **195**, 71–79.

46 Y. Xiao, L. Lu, A. Zhang, Y. Zhang, L. Sun, L. Huo and F. Li, Highly enhanced acetone sensing performances of porous and single crystalline ZnO nanosheets: high percentage of exposed (100) facets working together with surface modification with Pd nanoparticles, *ACS Appl. Mater. Interfaces*, 2012, **4**, 3797–3804.

47 Y. Deng, L. Tang, G. Zeng, C. Feng, H. Dong, J. Wang, H. Feng, Y. Liu, Y. Zhou and Y. Pang, Plasmonic resonance excited dual Z-scheme $BiVO_4$/Ag/Cu_2O nanocomposite: synthesis and mechanism for enhanced photocatalytic

performance in recalcitrant antibiotic degradation, *Environ. Sci.: Nano*, 2017, **4**, 1494–1511.

48 T.-T. Chen, I. C. Chang, M.-H. Yang, H.-T. Chiu and C.-Y. Lee, The exceptional photo-catalytic activity of ZnO/RGO composite via metal and oxygen vacancies, *Appl. Catal., B*, 2013, **142**, 442–449.

49 W. Wen, J.-M. Wu and Y.-D. Wang, Gas-sensing property of a nitrogen-doped zinc oxide fabricated by combustion synthesis, *Sens. Actuators, B*, 2013, **184**, 78–84.

50 C. A. Aggelopoulos, M. Dimitropoulos, A. Govatsi, L. Sygellou, C. D. Tsakiroglou and S. N. Yannopoulos, Influence of the surface-to-bulk defects ratio of ZnO and TiO_2 on their UV-mediated photocatalytic activity, *Appl. Catal., B*, 2017, **205**, 292–301.

51 R. Mueller, H. K. Kammler, K. Wegner and S. E. Pratsinis, OH surface density of SiO_2 and TiO_2 by thermogravimetric analysis, *Langmuir*, 2003, **19**, 160–165.

52 J. Xu, Z. Xue, N. Qin, Z. Cheng and Q. Xiang, The crystal facet-dependent gas sensing properties of ZnO nanosheets: experimental and computational study, *Sens. Actuators, B*, 2017, **242**, 148–157.

53 L. Van Hoang, T. Huynh Ngoc and S. H. Hur, Fabrication of 3D structured ZnO nanorod/reduced graphene oxide hydrogels and their use for photo-enhanced organic dye removal, *J. Colloid Interface Sci.*, 2015, **437**, 181–186.

54 Y. Xu and M. A. A. Schoonen, The absolute energy positions of conduction and valence bands of selected semiconducting minerals, *Am. Mineral.*, 2000, **85**, 543–556.

55 M. Hayyan, M. A. Hashim and I. M. AlNashef, Superoxide ion: generation and chemical implications, *Chem. Rev.*, 2016, **116**, 3029–3085.

56 L. K. Adams, D. Y. Lyon and P. J. J. Alvarez, Comparative eco-toxicity of nanoscale TiO_2, SiO_2, and ZnO water suspensions, *Water Res.*, 2006, **40**, 3527–3532.

57 M. Li, L. Zhu and D. Lin, Toxicity of ZnO Nanoparticles to *Escherichia coli*: Mechanism and the Influence of Medium Components, *Environ. Sci. Technol.*, 2011, **45**, 1977–1983.